



# Graphene-Based Field-Effect Photodetector with HgCdTe Absorber

Volodymyr Sheremet<sup>1</sup> · Md Fazle Rabbe<sup>1</sup> · Randy N. Jacobs<sup>2</sup> · Vitaliy Avrutin<sup>1</sup> · Ümit Özgür<sup>1</sup> · Nibir K. Dhar<sup>1</sup>

Received: 15 December 2023 / Accepted: 5 July 2024 / Published online: 17 July 2024  
© The Author(s) 2024

## Abstract

A field-effect photodetector structure composed of an Al<sub>2</sub>O<sub>3</sub>-encapsulated bilayer graphene conductive channel attached to an Al<sub>2</sub>O<sub>3</sub> dielectric layer deposited on a HgCdTe absorbing layer on CdTe/Si <211> was studied. Ti/Au ohmic contacts to the graphene layer were used as drain and source electrodes and back-gate voltage was applied to the Si substrate. It was demonstrated that 80% and 10% modulation of the graphene channel conductivity can be achieved under blue (50 W/cm<sup>2</sup>) and infrared (IR) (0.02 W/cm<sup>2</sup>) illumination, respectively, at a gate voltage of 7 V. Detector responsivity was measured as 406 A/W and 1.83 A/W under IR lamp and 405-nm laser irradiation, respectively, with corresponding gain values of 340 and 5.6. The detectivity of the 4 × 4 photodetector arrays was on the order of 10<sup>10</sup> Jones for the mid-wave infrared wavelength range (3–5 μm).

**Keywords** Photodetector · graphene · phototransistor · HgCdTe

## Introduction

Certain spectral ranges of infrared (IR) radiation can pass through gas and dust particles, and thus are used for terrestrial imaging/monitoring, exploration of objects in space, and IR communications. As it is absorbed by molecules and chemical bonds at characteristic resonances, IR radiation is also used for molecular analysis of the sample structure by Fourier transform IR (FTIR) spectroscopy. For terrestrial applications, primarily water and carbon dioxide absorption limit the atmospheric transparency windows to 1–2.5 μm in short-wave infrared (SWIR), 3–5 μm in mid-wave infrared (MWIR), and 8–14 μm in long-wave infrared (LWIR) spectral ranges, which are targeted for detector development for various applications.<sup>1</sup> The MWIR range in particular is important for distant thermal imaging.

Consumer IR imaging devices are commonly produced using thermal MWIR detectors<sup>1,2</sup> such as bolometers,<sup>3</sup> thermocouples,<sup>4</sup> and pyrometers,<sup>5</sup> which for example are represented in the product lines of the Teledyne FLIR, Honeywell, Hamamatsu, DIAS Infrared Systems, and many others, with application in a large variety of materials. They do not require active cooling and are characterized by small size, weight, power, and cost (SWaP-C). Photonic IR detectors, which provide much higher detectivity and higher speed, on the other hand, require cryogenic cooling to suppress thermal noise at the expense of increased SWaP-C.<sup>6</sup> Increasing the operating temperature of the IR photon detectors is thus a key objective.<sup>7</sup> HgCdTe, type II superlattices, two-dimensional (2D) materials, and colloidal quantum well (CQD)-based devices are considered promising for room-temperature operation.<sup>8</sup>

Hg<sub>x</sub>Cd<sub>1-x</sub>Te, which is the mainstay for high-performance MWIR and LWIR detectors, is a direct-bandgap ternary semiconductor with high charge carrier mobility and a low dielectric constant. For photodetection with high quantum efficiency, its energy bandgap can be tuned in a wide range corresponding to the wavelength region from 1 to 30 μm by varying the composition.<sup>9</sup> Recent efforts on HgCdTe-based IR photodetectors have focused primarily on increasing the operating temperature from cryogenic to room temperature.<sup>7</sup> At 300 K, because of the high intrinsic carrier concentration

✉ Volodymyr Sheremet  
sheremetv@vcu.edu

<sup>1</sup> Department of Electrical and Computer Engineering, Virginia Commonwealth University, 601 West Main Street, Richmond, VA 23284-3068, USA

<sup>2</sup> U.S. Army Combat Capabilities Development Command C5ISR Center, 10221 Burbeck Rd, Fort Belvoir, VA 22060, USA

of  $6 \times 10^{15} \text{ cm}^{-3}$  at MWIR and  $5 \times 10^{16} \text{ cm}^{-3}$  at LWIR, the minority carrier lifetime in HgCdTe is limited by Auger mechanisms.<sup>8</sup> Auger suppression is one of the approaches for reduction of dark current and increased detector operating temperature. For ideal Auger suppression, the electron concentration should be depleted, resulting in the removal of the free electrons from the absorber, which will suppress dark current.<sup>10</sup> To reach depletion of the absorber, one may apply reverse voltage, and a HgCdTe absorber with 5  $\mu\text{m}$  cutoff and  $10^{15} \text{ cm}^{-3}$  doping concentration would require 10–30 V of reverse voltage to be depleted. Such high voltage suppresses Auger recombination but creates excessive 1/f noise and thus dark current.<sup>7</sup> For the doping range of  $1\text{--}5 \times 10^{13} \text{ cm}^{-3}$ , full depletion of a 5- $\mu\text{m}$ -thick HgCdTe absorber may be achieved by applying 0–0.45 V, respectively.<sup>10</sup> Tedyne proposed a background-radiation-limited P-i-N HOT photodiode structure where a very low *n*-doped  $\sim 10^{13} \text{ cm}^{-3}$  absorber is surrounded by a wider-bandgap *p*-type buffer and *n*-type cap regions.<sup>10</sup> They also implemented fully depleted HgCdTe detectors for the high-operating-temperature (HOT) background-limited-performance (BLIP)  $640 \times 512$  focal plane arrays (FPAs) and presented their operation at up to 250 K.<sup>11</sup> The advantage of the fully depleted detectors increases with wavelength and temperature, as these parameters increase intrinsic carrier concentration, and for the SWIR range the advantage is small from the perspective of dark current or operating temperature.<sup>11</sup> According to Law 19, the detectivity of the P-i-N HgCdTe photodiodes with an absorber doping level of  $10^{13} \text{ cm}^{-3}$  at room temperature is limited by background radiation with  $D^* > 10^{10}$  Jones in the spectral range  $> 3 \mu\text{m}$ .<sup>8</sup>

One alternative to the HOT detector approach is interband and intersubband cascade devices.<sup>12</sup> It was predicted that superlattice-based devices have a lower Auger recombination coefficient than HgCdTe.<sup>13</sup> Devices based on 2D materials are considered promising for increased operating temperature as well.<sup>7,9,14–18</sup> The 2D materials offer unique properties in that the electronic states are easily tuned by the external field and bandgaps correlate with the number of layers and can range from 0 eV (graphene) to 6 eV (h-BN). Phototransistors based on 2D conductive channels have demonstrated enhanced performance.<sup>8</sup> A wide variety of 2D materials have been studied as a conductive channel for phototransistors, including graphene, transition metal dichalcogenides (TMDs), black phosphorus, and others. Silicon was used as a gate for such phototransistors with a SiO<sub>2</sub> insulator layer in most of these studies.<sup>19</sup> Significant attention has been focused on black phosphorus and its compounds<sup>14,15</sup> and TMDs.<sup>16,17</sup> Among the recently presented results, one of the highest detectivity values in the range of 3–5  $\mu\text{m}$  was observed for detectors based on a black phosphorus–arsenic alloy (bP-As), where detectivity of  $6 \times 10^{10}$  Jones and  $2.4 \times 10^{10}$  Jones was observed for the pure

b-P and b-PAs<sub>0.91</sub> at room temperature, respectively.<sup>14</sup> Detectivity of  $\sim 10^{10}$  Jones was reported for heterostructures based on 2D PdSe<sub>2</sub>-MoS<sub>2</sub> and bAsP-MoS<sub>2</sub> at room temperature in the range of 3–5  $\mu\text{m}$ .<sup>16</sup> Heterostructures of fluorographene/graphene were shown to exhibit detectivity on the order of  $2 \times 10^9$  Jones in the 3–5  $\mu\text{m}$  wavelength range.<sup>18</sup>

Despite these promising results, however, the application of these 2D materials is limited by their growth, as most of the devices studied so far were fabricated on chemical vapor deposition (CVD)-grown flakes.<sup>14–17</sup> Black phosphorus-based materials are also not stable in ambient conditions and require fabrication and passivation of the films in an inert atmosphere.<sup>14,15</sup>

Let us consider the principles of phototransistor operation consisting of a 2D channel with metal contacts on top of an absorbing semiconductor substrate. Photoconduction, photogating, and photovoltage effects have been shown to occur in structures with 2D conductive channels on a semiconductor substrate.<sup>19</sup> The semiconductor substrate absorbs most of the radiation, and photogenerated electron–hole pairs are separated by the applied gate voltage. Charge carriers in the interface of the semiconductor absorber create a photovoltage field that modulates channel conductivity and provides additional gain by extra charge carriers penetrating from the drain.<sup>19</sup> Absorption in 2D film also results in the photogeneration of charge carriers that provide photodetection. Trapping of the charge carriers by the interface states provides additional photogate voltage that modulates the channel current.

Graphene growth is the most mature technology among 2D materials, and its unique properties make it promising for detector development, with fast photoresponse, high detectivity/responsivity, and ultrabroad bandwidth at high operating temperatures. The bandgap of bilayer graphene is very sensitive to applied gate voltage,<sup>20–22</sup> which makes it promising for application in field-effect transistor development. However, since the absorption and carrier lifetime of graphene are limited, hybrid detector structures have been proposed with a graphene channel and HgCdTe absorber, where the graphene channel conductivity is modulated by the photogeneration in the HgCdTe absorber layer. Graphene/HgCdTe heterostructure photodetectors were studied previously where the *p*–*n* junction was realized by implementing *p*-type doped bilayer graphene onto *n*-HgCdTe.<sup>23–25</sup> This approach has limitations related to the surface states in HgCdTe, which can give rise to leakage, tunneling, and other phenomena that degrade the performance of the device.

In this work, we propose a field-effect detector with a HgCdTe photoabsorber and bilayer graphene conductive channel separated from the absorbing substrate by an insulating layer. Gate voltage applied to the HgCdTe absorber is used for the separation of the photogenerated charge carriers, and charge carriers in the proximity of the graphene channel

are used for modulating the graphene channel conductivity. This approach is expected to provide a room-temperature MWIR photodetector even with an undepleted, highly doped HgCdTe absorber.

## Experiment

Hg<sub>0.7</sub>Cd<sub>0.3</sub>Te/CdTe film on Si <211> substrate was received from the C5ISR Center, and bilayer graphene on Cu substrate was purchased from ACS Materials. A 20-nm-thick Al<sub>2</sub>O<sub>3</sub> layer was deposited on the surface of HgCdTe in an Ultratech Fiji G2 atomic layer deposition (ALD) system using trimethylaluminum (TMA) and water at 80°C. Such low-temperature deposition is required to prevent defect formation in the underlying HgCdTe film. Next, graphene was transferred to Al<sub>2</sub>O<sub>3</sub>/HgCdTe. During the transfer of graphene onto alumina, methyl group termination was used to achieve a hydrophobic surface and consequently improved adhesion of graphene to Al<sub>2</sub>O<sub>3</sub>.<sup>26</sup> A poly(methyl methacrylate) (PMMA) support film was used for the bilayer graphene transfer from the Cu foil to the Al<sub>2</sub>O<sub>3</sub>/HgCdTe/CdTe/Si <211> film. The Cu foil was etched in 0.2 M solution of ammonium persulfate after spin-coating and curing of the PMMA film. PMMA was dissolved in acetone after PMMA/graphene was transferred onto the Al<sub>2</sub>O<sub>3</sub>-coated HgCdTe/CdTe film.

Graphene conductive channels (10–150 μm width, 10–50 μm length) and ohmic contacts were defined by maskless photolithography with a Heidelberg μMLA aligner using AZ nLOF 2020 negative photoresist. E-beam/thermally evaporated Ti(15 nm)/Au (50 nm) metallization was utilized for the drain and source contacts. Graphene was then encapsulated by a 30-nm-thick ALD-grown Al<sub>2</sub>O<sub>3</sub>. Al<sub>2</sub>O<sub>3</sub> and graphene channel mesas were defined by inductively coupled plasma reactive ion etching (ICP-RIE) in a RIE-101iPH system in CF<sub>4</sub>(20 sccm)/Ar (5 sccm) chemistry at ICP and RIE power levels of 200 W and 70 W, respectively. This procedure resulted in the photodetector structure composed of a bilayer graphene conductive channel encapsulated by Al<sub>2</sub>O<sub>3</sub> and with Ti/Au drain–source contacts, which was separated from the Hg<sub>0.7</sub>Cd<sub>0.3</sub>Te absorber on Si substrate by a 20-nm-thick Al<sub>2</sub>O<sub>3</sub> insulating layer (Fig. 1).

The electron transport properties of HgCdTe layers were studied using a Lake Shore Cryogenics Hall effect measurement system. A Horiba LabRAM HR Evolution confocal Raman spectrometer was used for the characterization of the graphene/Al<sub>2</sub>O<sub>3</sub>/HgCdTe structure. A blue laser (405 nm) excitation with intensity of 50 W/cm<sup>2</sup> and SLS201L IR lamp excitation with intensity of 0.02 W/cm<sup>2</sup> were used for on-wafer photoresponse characterization of the detector structures on a probe station at room temperature. Optical

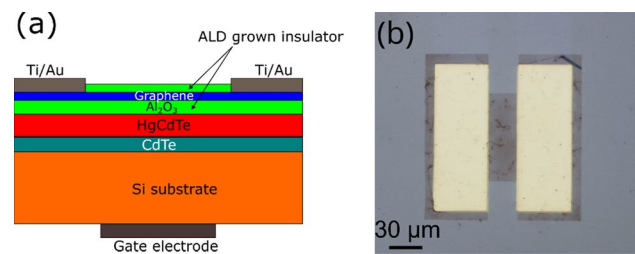


**Fig. 1** (a) Cross-sectional schematic and (b) top-view microscopic image of the field-effect graphene-based photodetector with HgCdTe absorber.

transmission was measured using a Thermo Scientific Nicolet iS50 Fourier transform infrared (FTIR) spectrometer.

The 4 × 4 photodetector arrays were fabricated and packaged into a chip carrier for the detailed photoresponse characterization under different light source excitation at room temperature. In addition to the previously used IR SLS201L lamp, the photodetectors were excited using continuous-wave (CW) laser (450 nm) and pulsed IR sources: a Ti:sapphire femtosecond laser (800-nm emission and 80-MHz repetition rate) and an optical parametric amplifier (OPA) with different frequency generation (1.2–12-μm emission and 1-kHz repetition rate) at room temperature.

## Results and Discussion

To understand the device operation, it is necessary to determine the charge carrier density and mobility values in graphene and HgCdTe. The Hall measurements revealed that bilayer graphene transferred onto the Al<sub>2</sub>O<sub>3</sub>-coated sapphire had a degenerate *p*-type conductivity with sheet carrier density of  $2 \times 10^{13} \text{ cm}^{-2}$  and mobility of  $950 \text{ cm}^2 \text{ V}^{-1} \text{ s}^{-1}$  (Fig. 2a). The HgCdTe layer exhibited *n*-doping with a sheet carrier density of  $5 \times 10^{12} \text{ cm}^{-2}$  and mobility of  $4200 \text{ cm}^2 \text{ V}^{-1} \text{ s}^{-1}$  at room temperature. Temperature-dependent measurements of the *n*-HgCdTe showed a decrease in the sheet carrier density by one order of magnitude and mobility that was nearly doubled for temperatures below 150 K, which may be explained by partial freeze-out of the charge carriers. After graphene was transferred onto the Al<sub>2</sub>O<sub>3</sub>-coated surface of HgCdTe, the electrical characteristics of the hybrid structure correlated closely with those of HgCdTe. The optical transmission of the HgCdTe/CdTe/Si epitaxial structure indicated a cutoff wavelength of  $\sim 4.5 \mu\text{m}$  (Fig. 2b).

The *p*-type conductivity of the bilayer graphene is likely related to the strain state of the layer that was assessed by the Raman spectroscopy.<sup>27</sup> The Raman spectra of the HgCdTe/CdTe/Si before and after graphene transfer are presented in

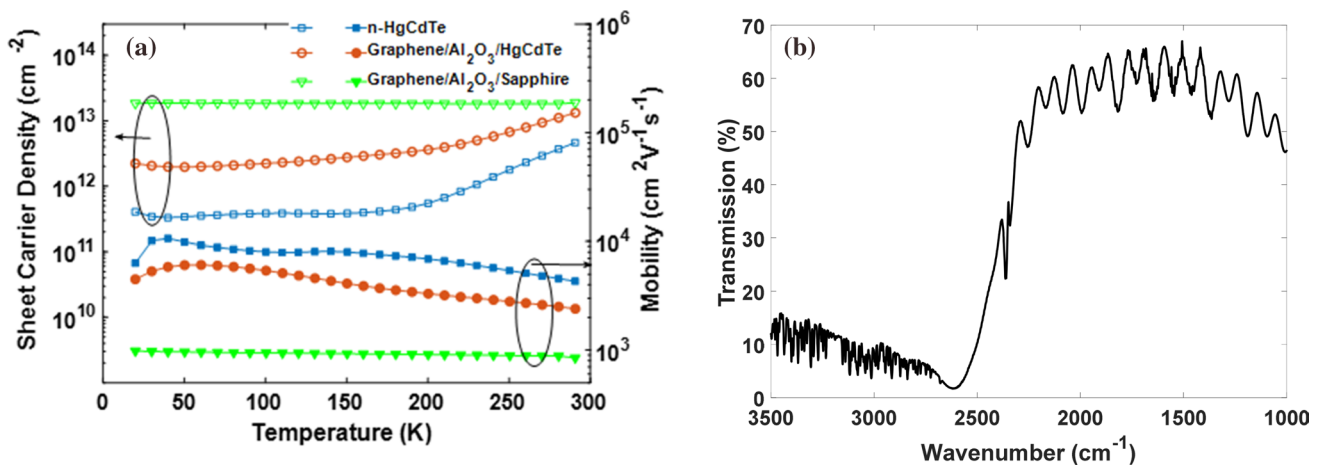


**Fig. 2** (a) Sheet carrier density and mobility dependence on the temperature measured by the Hall technique for the *n*-HgCdTe film, bilayer graphene on Al<sub>2</sub>O<sub>3</sub>-coated sapphire, and graphene/Al<sub>2</sub>O<sub>3</sub>/

HgCdTe structure and (b) transmission spectrum for the HgCdTe/CdTe/Si epitaxial structure.

**Fig. 3a.** The HgCdTe layer exhibits the characteristic phonon peaks [149 cm<sup>-1</sup> (TO<sub>1</sub>), 121 cm<sup>-1</sup> (TO<sub>2</sub>), 155 cm<sup>-1</sup> (LO<sub>2</sub>)], *D* peak at 107 cm<sup>-1</sup>, and *A* peak at 134 cm<sup>-1</sup>.<sup>28</sup> After the film transfer, one can observe the characteristic graphene peaks at 1578 cm<sup>-1</sup> (*G*) and 2670 cm<sup>-1</sup> (2*D*) in addition to those related to HgCdTe.<sup>29,30</sup> The peak at 1580 cm<sup>-1</sup> is associated with the in-plane vibrational mode of sp<sup>2</sup> hybridized carbon atoms, and the peak at 2677 cm<sup>-1</sup> corresponds to the second-order double-resonance process involving two phonons and is sensitive to the number of graphene layers.<sup>31</sup> For the bilayer graphene, the ratio of 2*D* and *G* peak intensities is expected to be 1 as observed in our experiment.<sup>31</sup> The dependence of the 2*D* and *G* bilayer graphene characteristic Raman spectra peak positions on the strain has been reported

elsewhere.<sup>27,29,31</sup> The strain value which defines sheet carrier density in graphene can be determined from the exact *G* and 2*D* frequencies (Fig. 3b).<sup>27</sup> This procedure indicated strain of 0.18% and sheet carrier density of 10<sup>13</sup> cm<sup>-2</sup> in the film of bilayer graphene on Al<sub>2</sub>O<sub>3</sub>-coated HgCdTe (Fig. 3b).

Drain–source *I*–*V* measurements in the range of –1 V to 5 V demonstrate conduction modulation in the graphene channel that is much stronger with the HgCdTe absorber than without it under 405-nm laser irradiation (Fig. 4a). The dependence of the average modulation on the channel width demonstrates an increase in modulation from 3% up to 45% when the channel width increases from 10 μm to 70 μm under IR lamp illumination, and from 35% to 50% when the channel width increases from 10 μm to 130 μm

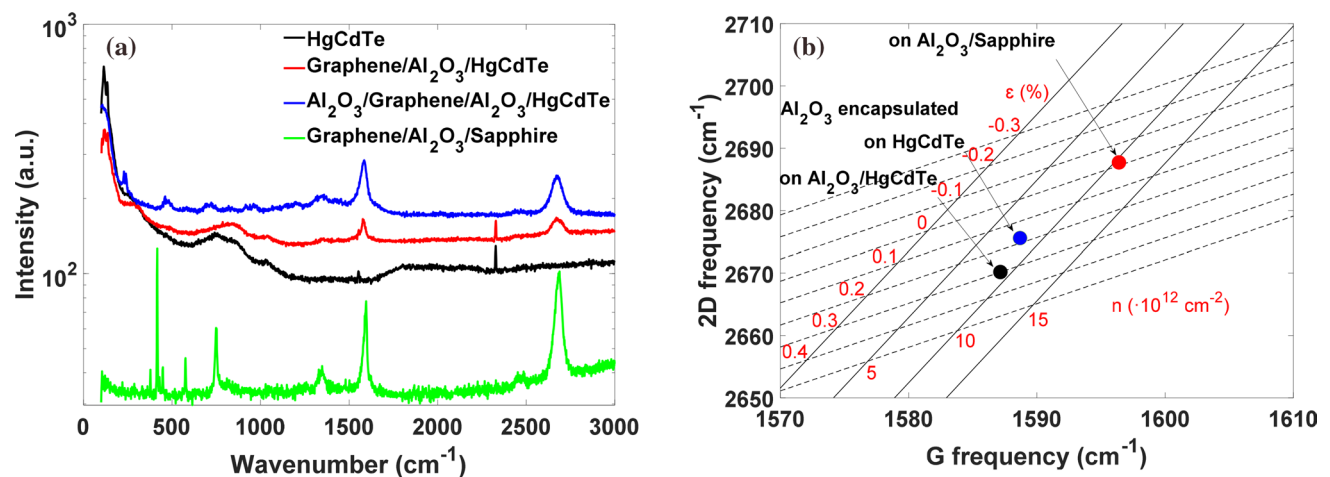


**Fig. 3** (a) Raman spectra of graphene/Al<sub>2</sub>O<sub>3</sub>/HgCdTe/CdTe/Si with and without Al<sub>2</sub>O<sub>3</sub> encapsulation compared against spectra for HgCdTe/CdTe/Si and graphene/Al<sub>2</sub>O<sub>3</sub>/sapphire. (b) 2*D* frequency versus *G* frequency dependence for graphene with various strain and

charge carrier density values (data for strain and corresponding carrier densities are from Ref. 27). The solid symbols indicate the values measured by Raman spectroscopy for the layers used in this study.

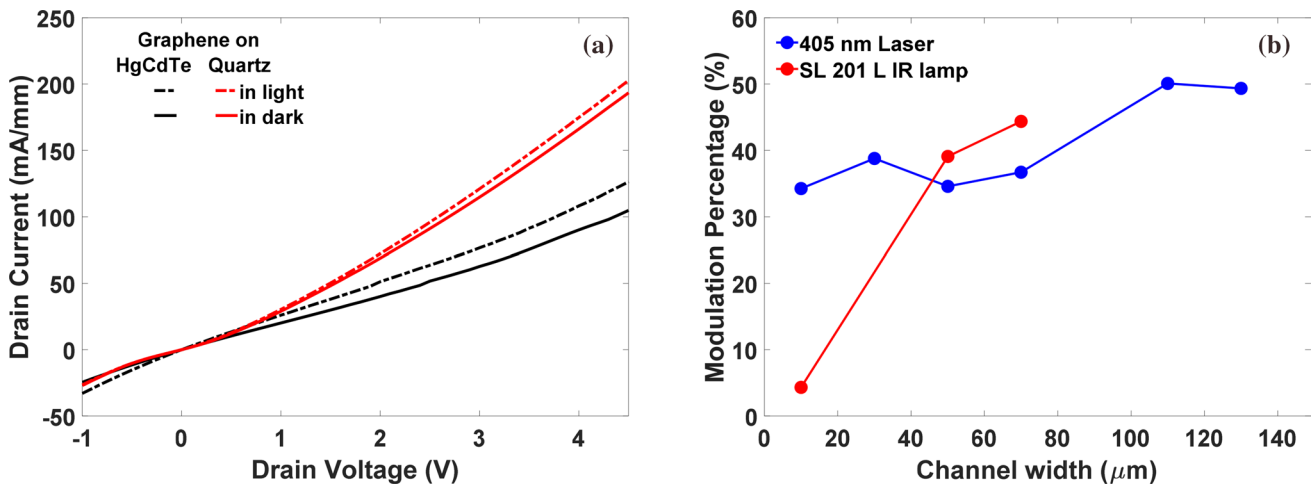


**Fig. 4** (a) Drain–source  $I_{DS}$ – $V_{DS}$  characteristics of graphene on quartz and graphene on HgCdTe with and without focused CW blue laser (405 nm) illumination, and (b) dependence of graphene channel mod-

ulation on the channel width under 405-nm laser and IR lamp exposure measured under a probe station at room temperature.

under 405-nm laser irradiation (Fig. 4b). For a channel width of 30 μm, modulation of 80% and 10% was achieved for 405-nm and IR illumination, respectively, with gate voltage increased to 7 V (Fig. 5).

The channel modulation is dependent on the gate voltage applied, as expected. The highest detector responsivity of 1.83 A/W and 406 A/W were observed at a gate voltage of 7 V, which provides a gain of 5.6 and 340 for 405-nm laser and SLS201L IR lamp irradiation, respectively (Fig. 6).

To further evaluate the device prospects, the response of 4 × 4 detector arrays packaged into a chip carrier was measured at different excitation wavelengths. From the results presented above, a graphene-based field-effect photodetector

with a HgCdTe absorber having a 150 × 50 μm channel was chosen as the most promising for the array. The corresponding devices were fabricated according to the processes described above with an additional step for the deposition of contact pads and transfer lines (Fig. 7). Four contact pads connected to the source terminals and four contact pads connected to the drain terminals were used to connect to each photodetection structure. Fabricated wafers were attached to the chip carrier by applying Chemtronics CW2460 conductive epoxy.

The photodetectors on the array were studied under excitation from light sources with different emission wavelengths. Devices in the array were operated at  $V_{DS} = 5$  V and  $V_{GS} = 7$  V. Excitation was modulated with an optical

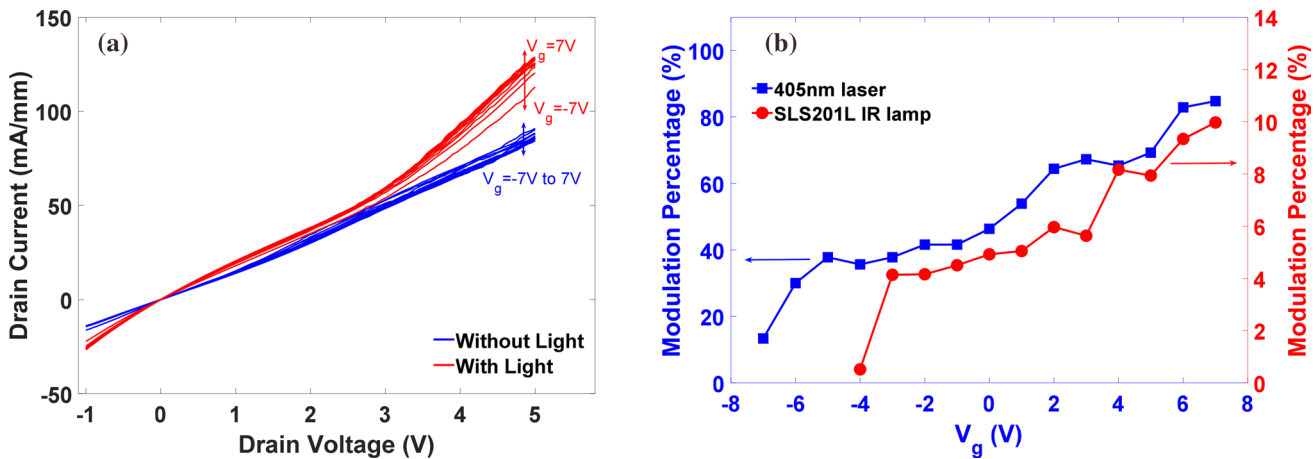


**Fig. 5** (a)  $I_{DS}$ – $V_{DS}$  characteristics of graphene channel (10 × 30 μm) with and without focused CW 405-nm laser illumination at  $V_g = -7$  V to 7 V and (b) conductivity modulation of graphene channel (10 ×

50 μm) as a function of the back-gate voltage measured under a probe station at room temperature.

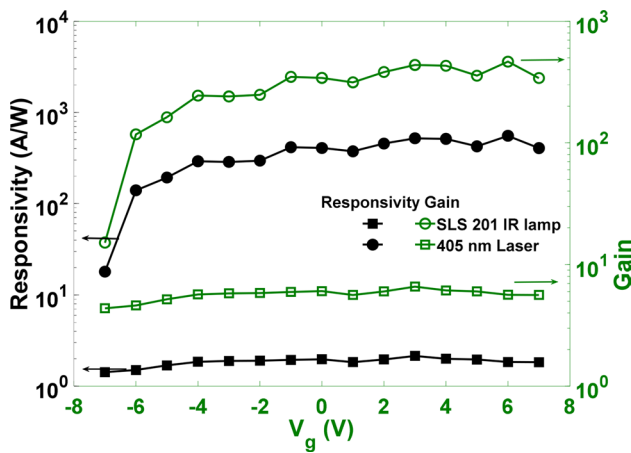


**Fig. 6** Responsivity and gain of the studied  $\text{Al}_2\text{O}_3/\text{graphene}/\text{Al}_2\text{O}_3/\text{HgCdTe}/\text{CdTe}/\text{Si}$  detector under focused 405-nm laser and IR lamp excitation at room temperature.

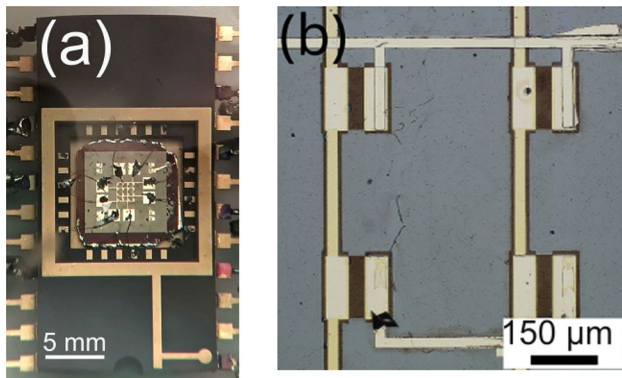


**Fig. 7** (a) Photo of the graphene-based field-effect photodetector  $4 \times 4$  array with HgCdTe adsorber packaged in chip-carrier and (b) magnified image of the detector structures.

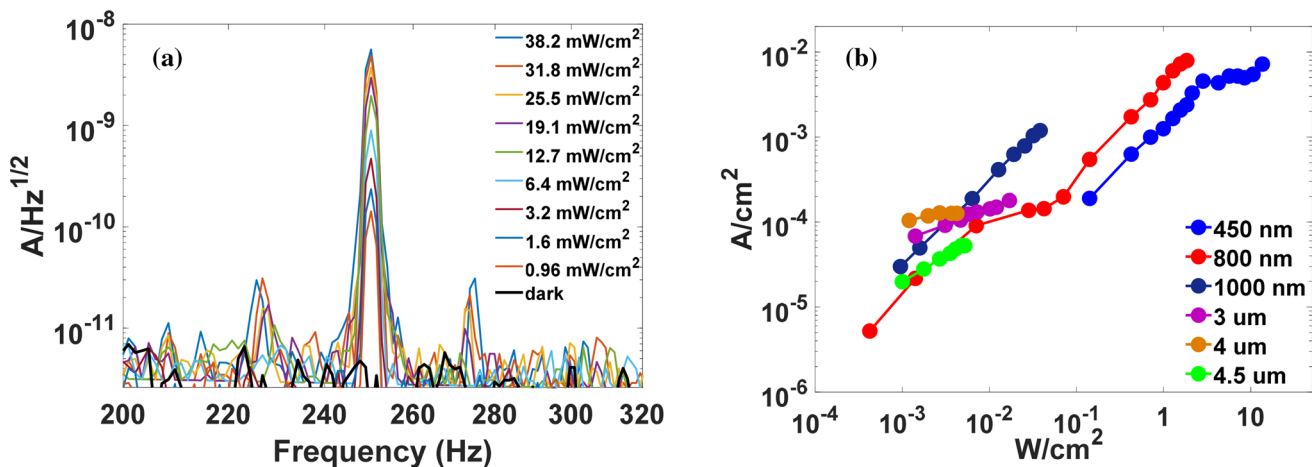


**Fig. 8** (a) Spectrum analysis of the photodetector array output under IR lamp excitation with different power density values and (b) dependence of photogenerated current on the excitation power intensity for the studied excitation source wavelengths measured at room temperature.

chopper except for the 1-kHz OPA excitation, and an attenuator was used for varying the excitation light power. The current through the detector was assessed from the voltage drop across a  $1 \text{ M}\Omega$  shunt resistor connected in series with the drain–source of the field-effect photodetector. Signals were amplified with an Stanford Research Systems SR560 low-noise preamplifier, with output read by a Tektronix TDS2024B oscilloscope. The modulated signal and fast Fourier transform (FFT) were used for the spectrum analysis of the detector output under excitation.

An example of the device current spectrum under variable excitation from the SLS201L IR lamp is presented in Fig. 8a. The current spectra of the photodetector were analyzed for different excitation sources and provided information about the output signal of the device and dark current noise level ( $i_n$ ) of the system. The results achieved for different excitation sources are presented in Table I.

The photogenerated current density versus the excitation power density exhibits a linear dependence for nearly all excitation sources (Fig. 8b). The response measured with the 450-nm CW laser tends to saturate at power density greater than  $1 \text{ W}/\text{cm}^2$ . The increment rate with excitation density is lower for the 1-kHz IR laser excitations ( $3 \mu\text{m}$ ,  $4 \mu\text{m}$ ,  $4.5 \mu\text{m}$ ), most likely as a result of orders-of-magnitude higher pulse power of the excitation.

The responsivity of the photodetector under different excitation conditions is presented in Fig. 9a. As expected, the device responsivity is higher at longer excitation wavelengths up to the cutoff wavelength ( $\sim 4.5 \mu\text{m}$ ), owing to the higher photon flux density for the same emission power in lower-energy excitation. The maximum responsivity increases from  $1.6 \text{ mA}/\text{W}$  under 450-nm excitation to  $86.9 \text{ mA}/\text{W}$  under  $4\text{-}\mu\text{m}$  excitation. Although it does not change with excitation fluence at lower irradiance levels,

**Table I** Parameters of the studied graphene-based field-effect photodetector 4 × 4 array with HgCdTe adsorber achieved at room temperature

	$R$ (A/W)	$i_n$ , A/Hz <sup>1/2</sup>	NEP (W)	$D^*$ (Jones)
450 nm CW laser	$1.6 \times 10^{-3}$	$5 \times 10^{-12}$	$3.11 \times 10^{-9}$	$6.22 \times 10^6$
800 nm Ti:sapphire laser 80 MHz	$15.4 \times 10^{-3}$	$2 \times 10^{-12}$	$1.30 \times 10^{-10}$	$1.49 \times 10^8$
1 μm SLS201L IR lamp	$32.7 \times 10^{-3}$	$2 \times 10^{-12}$	$6.12 \times 10^{-11}$	$3.16 \times 10^8$
3 μm Solstice Ace laser system	$48.2 \times 10^{-3}$	$2 \times 10^{-13}$	$4.15 \times 10^{-12}$	$2.09 \times 10^{10}$
4 μm Solstice Ace laser system	$86.8 \times 10^{-3}$	$3 \times 10^{-13}$	$3.45 \times 10^{-12}$	$2.51 \times 10^{10}$
4.5 μm Solstice Ace laser system	$19.8 \times 10^{-3}$	$2 \times 10^{-13}$	$1.01 \times 10^{-11}$	$8.56 \times 10^9$

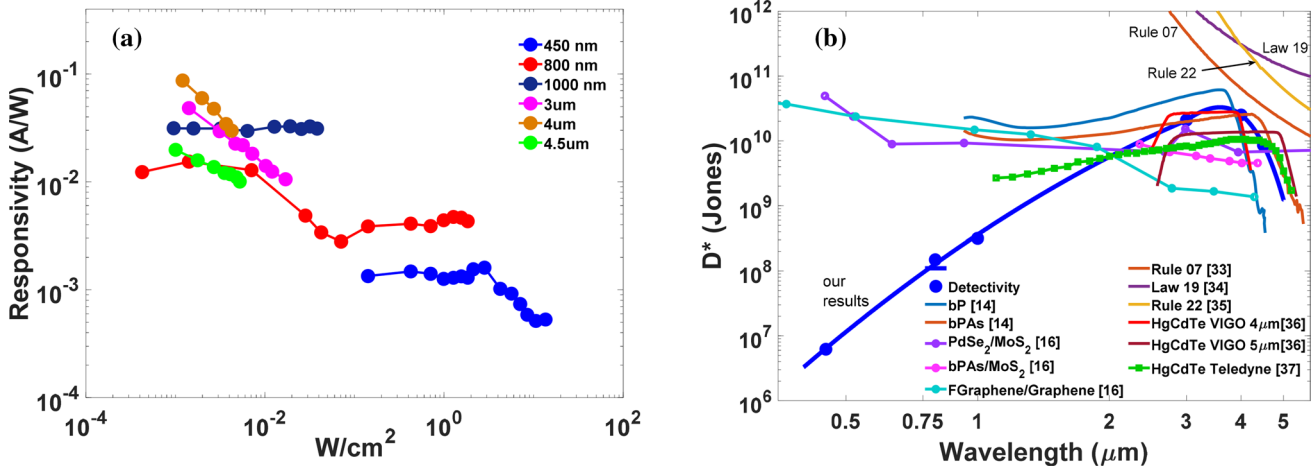


**Fig. 9** (a) Dependence of responsivity on the power density and (b) dependence of detectivity on the excitation wavelength of the photodetectors in the array at room temperature.

similar to the case of the IR incandescent lamp, responsivity consistently decreases with excitation for all pulsed sources used as well as for the CW 450-nm excitation beyond the 2–3 W/cm<sup>2</sup> power density. This is most likely related to the saturation of the response which can result from heating, because the pulsed IR laser sources used for this study have high pulse energy, i.e. much higher instantaneous power than the CW sources. The noise-equivalent power (NEP) and detectivity ( $D^*$ ) of the detectors can be calculated according to the following formula.<sup>32</sup>

$$NEP = \frac{i_n}{R} \tag{1}$$

$$D^* = \frac{\sqrt{AB}}{NEP}, \tag{2}$$

where NEP is noise-equivalent power,  $i_n$  is the dark current noise level,  $R$  is responsivity,  $D^*$  is detectivity,  $A$  is the area of the detector, and  $B$  is bandwidth.

The maximum detectivity for the different excitation wavelengths used is shown in Fig. 9b. It increases from  $6.22 \times 10^6$  Jones under 450-nm excitation to  $2.51 \times 10^{10}$  Jones under 4-μm excitation. When the excitation wavelength

approaches the cutoff, the detectivity decreases to  $8.56 \times 10^9$  Jones at 4.5 μm and further by a factor of 2 at 4.7 μm. The calculated responsivity, NEP, and detectivity values are provided in Table I. The detectivity results are compared in Fig. 9b with Rule 07,<sup>33</sup> Rule 22,<sup>34</sup> and Law 19<sup>35</sup> proposed by Teledyne for the characterization of the HgCdTe device performance. The detectivity values of the HgCdTe p-i-n photodiodes optically immersed with the help of micro-lenses from VIGO<sup>36</sup> as well as photodiodes presented by Teledyne<sup>37</sup> are also included in the comparison. In addition, Fig. 9b includes the results from recently demonstrated black phosphorus,<sup>14</sup> MoS<sub>2</sub>,<sup>16</sup> and fluorographene/graphene heterostructure-based devices. As one can see, the results presented in our work are comparable to those presented in other publications and can be achieved with high doping of the HgCdTe of  $\sim 10^{16}$  cm<sup>-3</sup>.

Using optical modulation or pulsed excitation, the time response of the photodetector structures was also evaluated. A representative example of photocurrent for 250 Hz modulation with 800-nm Ti:sapphire femtosecond laser excitation at 662 mW/cm<sup>2</sup> power density is presented in Fig. 10a, showing a rise time of 340 μs, resulting primarily from the optical chopper. Under 3-μm femtosecond pulse excitation

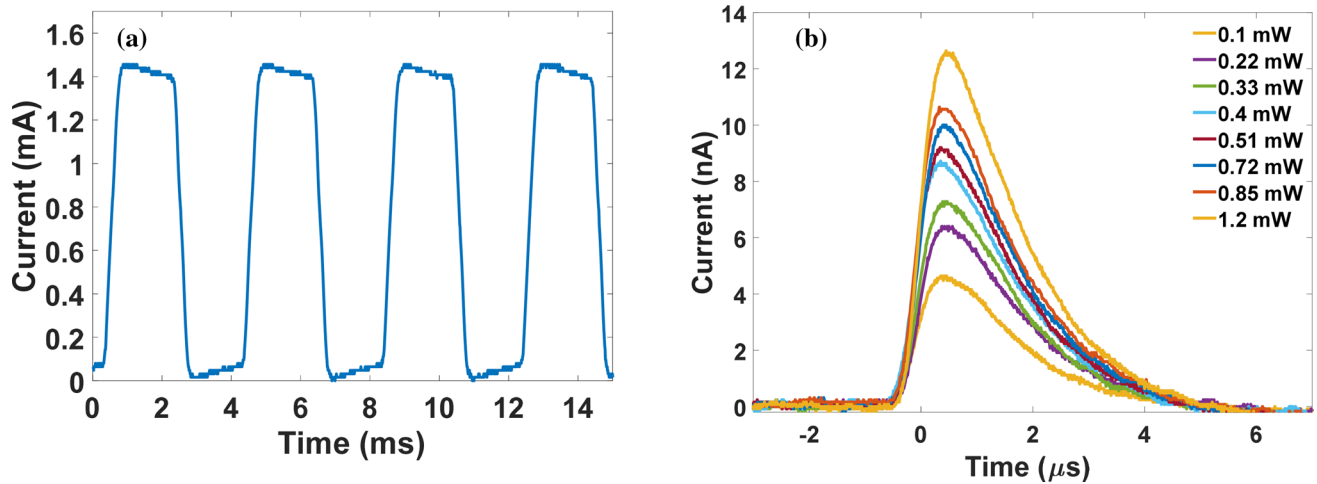


**Fig. 10** Current output of the photodetector with time for (a) 800-nm Ti:sapphire modulated excitation with 250 Hz modulation and (b) 3- $\mu\text{m}$  femtosecond OPA pulsed excitation.

at 1 kHz, a rise time of 0.5  $\mu\text{s}$  and fall time of 2.74  $\mu\text{s}$  were measured, as shown in Fig. 10b.

The data presented indicate the feasibility of the proposed approach for developing novel room-temperature photodetectors for the MWIR wavelength range. This device configuration will be further optimized by developing an efficient insulating layer between the conductive channel and photoabsorber that will provide high modulation.

## Conclusion

Graphene-based field-effect photodetectors with a HgCdTe absorber were fabricated, and conduction modulation of 80% and 10% at a gate voltage of 7 V were achieved for blue (50 W/cm<sup>2</sup>) and IR (0.02 W/cm<sup>2</sup>) illumination, respectively. Although these measurements are not optimized for the HgCdTe bandgap under study, they indicate the potential for a new IR detector design with high transconductance gain in the transistor channel. Responsivity values of 1.83 A/W and 406 A/W were estimated at the gate voltage of 7 V, providing a gain of 5.6 and 340 for 405-nm laser and SLS201L IR lamp irradiation, respectively, for the on-wafer devices. Detectivity in the order of  $\sim 10^{10}$  Jones was demonstrated for the room-temperature operation of devices in the packaged array for the MWIR (3–5  $\mu\text{m}$ ) wavelength range.

**Acknowledgments** The authors are grateful to David Pate and Adam Ball from Virginia Commonwealth University for their support in organizing the optical characterization of the detector structures.

**Conflict of interest** The authors declare that they have no conflict of interest.

**Open Access** This article is licensed under a Creative Commons Attribution 4.0 International License, which permits use, sharing, adaptation, distribution and reproduction in any medium or format, as long as you give appropriate credit to the original author(s) and the source, provide a link to the Creative Commons licence, and indicate if changes were made. The images or other third party material in this article are included in the article's Creative Commons licence, unless indicated otherwise in a credit line to the material. If material is not included in the article's Creative Commons licence and your intended use is not permitted by statutory regulation or exceeds the permitted use, you will need to obtain permission directly from the copyright holder. To view a copy of this licence, visit <http://creativecommons.org/licenses/by/4.0/>.

## References

1. A. Rogalski and Z. Bielecki, *Detection of Optical Signals* (Boca Raton: CRC Press, 2022).
2. P.W. Kruse, *Uncooled Thermal Imaging Arrays, Systems, and Applications* (Bellingham: SPIE Press, 2001).
3. J.L. Tissot, C. Trouilleau, B. Fieque, A. Crastes, and O. Legras, Uncooled microbolometer detector: recent developments at ULIS. *Opto-Electron. Rev.* 14, 25 (2006).
4. M. Abe, Y. Abe, N. Kogushi, K.S. Ang, R. Hofstetter, H. Wang, and G.I. Ng, High-performance modulation-doped AlGaAs/InGaAs thermopiles for uncooled infrared FPA application. *Infrared Phys. Technol.* 59, 182 (2013).
5. N. Neumann, M. Ebermann, K. Schreiber, and M. Heinze, *Multi-colour and Tunable-Colour Pyroelectric Detectors* (Dresden: InfraTec GmbH, 2008).
6. A. Rogalski, History of infrared detectors. *Opto-Electron. Rev.* 20, 279 (2012).
7. A. Rogalski, P. Martyniuk, M. Kopytko, and W. Hu, Trends in performance limits of the HOT infrared photodetectors. *Appl. Sci.* 11, 501 (2021).
8. A. Rogalski, M. Kopytko, W. Hu, and P. Martyniuk, Infrared HOT photodetectors: status and outlook. *Sensors* 23, 7564 (2023).
9. A. Rogalski, HgCdTe infrared detector material: history, status and outlook. *Rep. Prog. Phys.* 68, 2267 (2005).



10. D. Lee, M. Carmody, E. Piquette, P. Dreiske, A. Chen, A. Yulius, D. Edwall, S. Bhargava, M. Zandian, and W.E. Tennant, High-temperature HgCdTe: a vision for the near future. *J. Electron. Mater.* 45, 4587 (2016).
11. P. Jerrama and J. Beletic, Teledyne's high performance infrared detectors for space missions. *Proc. SPIE* 11180, 111803D–1 (2018).
12. W. Huang, S.M.S. Rassel, L. Lia, J.A. Massengale, R.Q. Yanga, T.D. Mishima, and M.B. Santos, A unified figure of merit for interband and intersubband cascade devices. *Infrared Phys. Technol.* 96, 298 (2019).
13. D. Lee, P. Dreiske, J. Ellsworth, R. Cottier, A. Chen, and S. Tallaricao, Law 19—the ultimate photodiode performance metric. *Proc. SPIE* 11407, 114070X (2020).
14. M. Amani, E. Regan, J. Bullock, G.H. Ahn, and A. Javey, Mid-wave infrared photoconductors based on black phosphorus-arsenic alloys. *ACS Nano* 11, 11724 (2017).
15. M. Long, A. Gao, P. Wang, H. Xia, C. Ott, C. Pan, Y. Fu, E. Liu, X. Chen, W. Lu, T. Nilges, J. Xu, X. Wang, W. Hu, and F. Miao, Room temperature high-detectivity mid-infrared photodetectors based on black arsenic phosphorus. *Sci. Adv.* 3, e1700589 (2017).
16. M. Long, Y. Wang, P. Wang, X. Zhou, H. Xia, C. Luo, S. Huang, G. Zhang, H. Yan, Z. Fan, X. Wu, X. Chen, W. Lu, and W. Hu, Palladium diselenide long-wavelength infrared photodetector with high sensitivity and stability. *ACS Nano* 13, 2511 (2019).
17. L. Zeng, D. Wu, J. Jie, X. Ren, X. Hu, S. Lau, Y. Chai, and Y.H. Tsang, Van der Waals epitaxial growth of mosaic-like 2D platinum ditelluride layers for room-temperature mid-infrared photo-detection up to 10.6  $\mu\text{m}$ . *Adv. Mater.* 32, 2004412 (2020).
18. S. Du, W. Lu, A. Ali, P. Zhao, K. Shehzad, H. Guo, L. Ma, X. Liu, X. Pi, P. Wang, H. Fang, Z. Xu, C. Gao, Y. Dan, P. Tan, H. Wang, C.-T. Lin, J. Yang, S. Dong, Z. Cheng, E. Li, W. Yin, J. Luo, B. Yu, T. Hasan, Y. Xu, W. Hu, and X. Duan, A broadband fluorographene photodetector. *Adv. Mater.* 29, 1700463 (2017).
19. H. Fang and W. Hu, Photogating in low dimensional photodetectors. *Adv. Sci.* 4, 1700323 (2017).
20. A. Bostwick, J. McChesney, T. Ohta, E. Rotenberg, T. Seyller, and K. Horn, Experimental studies of the electronic structure of graphene. *Prog. Surf. Sci.* 84, 380 (2009).
21. A.K. Sood, I. Lund, Y.R. Puri, H. Efstathiadis, P. Haldar, N.K. Dhar, J. Lewis, M. Dubey, E. Zakar, P. Wijewarnasuriya, D.L. Polla, and M. Fritze, Review of graphene technology and its applications for electronic devices, *Graphene-New Trends and Developments*. ed. F. Ebrahimi (London: Intech Open, 2015).
22. B.N. Szafranek, G. Fiori, D. Schall, D. Neumaier, and H. Kurz, Current saturation and voltage gain in bilayer graphene field effect transistors. *Nano Lett.* 12, 1324–1328 (2012).
23. S. Bansal, K. Sharma, P. Jain, N. Sardana, S. Kumar, N. Gupta, and A.K. Singh, Bilayer graphene/HgCdTe based very long infrared photodetector with superior external quantum efficiency, responsivity, and detectivity. *RSC Adv.* 8, 39579 (2018).
24. A.K. Sood, J.W. Zeller, P. Ghuman, S. Babu, N.K. Dhar, R.N. Jacobs, S. Ganguly, S. Ahmed, F. Tonni, A. Ghosh, L.S. Chaudhary, and H. Efstathiadis, Development of high-performance graphene-HgCdTe detector technology for mid-wave infrared applications. *Proc. SPIE* 12091, 1209108–1209111 (2022).
25. A.K. Sood, J.W. Zeller, P. Ghuman, S. Babu, N.K. Dhar, S. Ganguly, L.S. Chaudhary, and H. Efstathiadis, High-performance graphene-enhanced HgCdTe photodetectors for uncooled mid-wave infrared sensing. *Proc. SPIE* 12430, 124300U–1 (2023).
26. D.-W. Park, S. Mikael, T.-H. Chang, S. Gong, and Z. Ma, Bottom-gate coplanar graphene transistors with enhanced graphene adhesion on atomic layer deposition  $\text{Al}_2\text{O}_3$ . *Appl. Phys. Lett.* 106, 102106 (2015).
27. J.E. Lee, G. Ahn, J. Shim, Y.S. Lee, and S. Ryu, Optical separation of mechanical strain from charge doping in graphene. *Nat. Commun.* 3, 1024 (2022).
28. P. Amirtharaj, N.K. Dhar, J. Baars, and H. Seelewind, Investigation of photons in HgCdTe using Raman scattering and far-infrared reflectivity. *Semicond. Sci. Technol.* 5, S68 (1990).
29. F. Comanescu, A. Istrate, and M. Purica, Assessing by Raman spectroscopy the quality of CVD graphene transferred on oxidized silicon and quartz substrates. *Rom. J. Inf. Sci. Technol.* 22, 30 (2019).
30. S. Ushiba, T. Ono, Y. Kanai, K. Inoue, M. Kimura, and K. Matsumoto, Graphene as an imaging platform of charged molecules. *ACS Omega* 3, 3137 (2018).
31. S. Sahoo, R. Palai, and R.S. Katiyar, Polarized Raman scattering in monolayer, bilayer and suspended bilayer graphene. *J. Appl. Phys.* 110, 044320 (2011).
32. Y. Fang and J. Huang, Resolving weak light of sub-picowatt per square centimeter by hybrid perovskite photodetectors enabled by noise reduction. *Adv. Mater.* 27, 2804–2810 (2015).
33. W.E. Tennant, D. Lee, M. Zandian, E. Piquette, and M. Carmody, MBE HgCdTe technology: a very general solution to IR detection, described by “Rule 07”, a very convenient heuristic. *J. Electron. Mater.* 37, 1406 (2008).
34. M. Zandian, Rule-22: an update to Rule-07. *J. Electron. Mater.* 52, 7095 (2023).
35. D. Lee, P. Dreiske, J. Ellsworth, R. Cottier, A. Chen, S. Tallaricao, A. Yulius, M. Carmody, E. Piquette, M. Zandian, and S. Douglas, Law 19—the ultimate photodiode performance metric. *Proc. SPIE* 11407, 114070X (2020).
36. Available online: <https://vigo.com.pl/wp-content/uploads/2017/06/VIGO-Catalogue.pdf>
37. Available online: <https://www.teledynejudson.com/news/Documents/HOT%20MCT%20new%20product%20charts%20FINAL.pdf>

**Publisher's Note** Springer Nature remains neutral with regard to jurisdictional claims in published maps and institutional affiliations.